How to cite: *Angew. Chem. Int. Ed.* **2021**, *60*, 21449–21456
International Edition: doi.org/10.1002/anie.202107265
German Edition: doi.org/10.1002/ange.202107265

Cancer Therapy | Hot Paper

$\{BiW_8O_{30}\}$ Exerts Antitumor Effect by Triggering Pyroptosis and Upregulating Reactive Oxygen Species

Di Jia[+], Lige Gong[+], Ying Li, Shu Cao, Weiming Zhao, Lijun Hao, Shasha Li, Bo Pang, Chunjing Zhang, Shuyan Li, Wei Zhang, Tianyi Chen, Limin Dong, Baibin Zhou, and Dan Yang**

Abstract: *We successfully synthesized* ***{BiW$_8$}****, a 10-nuclear heteroatom cluster modified {BiW$_8$O$_{30}$}. At 24 h post-incubation, the IC$_{50}$ values of* ***{BiW$_8$}*** *against HUVEC, MG63, RD, Hep3B, HepG2, and MCF7 cells were 895.8, 127.3, 344.3, 455.0, 781.3, and 206.3 μM, respectively. The IC$_{50}$ value of* ***{BiW$_8$}*** *on the MG63 cells was more than 2-fold lower than that of the other raw materials. Through morphological and functional features, we demonstrated pyroptosis as a newly identified mechanism of cell death induced by* ***{BiW$_8$}****.* ***{BiW$_8$}*** *increased 2-fold reactive oxygen species (ROS) levels in MG63 cells at 24 h post-incubation. Compared with 0 h, the glutathione (GSH) content decreased by 59, 65, 75, 94, and 97% at 6, 12, 24, 36 and 48 h post-incubation, respectively. Furthermore, multiple antitumor mechanisms of* ***{BiW$_8$}*** *were identified via transcriptome analysis and chemical simulation, including activation of pyroptosis, suppression of GSH generation, depletion of GSH, and inhibition of DNA repair.*

Introduction

Polyoxometalates (POMs) have unmatched multifunctional chemical properties with well-defined structures, regular sizes, superior redox properties,[1,2] high solubility,[3–5] stability,[6] and other advantages under a wide range of pH. It is widely used in fields such as pharmaceutical medicine.[7] Furthermore, it is a class of outstanding cluster compounds formed by pre-transition metal ions linked by oxygen ions.[8–11] Despite being known to demonstrate anticancer activity for more than 50 years, it remains challenging to understand their underlying mechanism. Specifically, the antitumor mechanisms behind the cell death and cell fate decisions of POMs have not been well studied.

We summarized the major events involved in the anticancer activity of POMs via cell death found in literature (Figure 1, Table S2). Among these reports, only a few described apoptosis and necrosis. However, most reports did not describe the manner of cell death. Moreover, little is known about the molecular mechanisms of POM-induced cell death.[12–15] In recent years, there has been increasing research on new mechanisms involving cell death, such as pyroptosis and ferroptosis.[16] These newly discovered mechanisms have also started being considered promising antitumor mechanisms for the development of chemotherapeutic drugs.[17] Exploring novel mechanisms of POM-induced cell death may aid in providing evidence to support the potential value of POMs in clinical applications. Pyroptosis is a novel form of regulated cell death (RCD) that differs from apoptosis, necrosis, and other types of cell death. It is characterized by the formation of plasma membrane pores by members of the gasdermin protein family, causing the release of cell contents, such as LDH and inflammatory cytokines.[18] It has been found that pyroptosis can play an important role in tumor chemotherapy as a prospective cell death pathway because of its ability to trigger antitumor immune responses.[19–21]

[*] Dr. D. Jia,[+] Prof. Dr. C. Zhang, Prof. Dr. S. Li
Department of Biochemistry and Molecular Biology, Qiqihar Medical University
Qiqihar 161006 (China)

Y. Li, S. Cao, W. Zhang, T. Chen, Prof. Dr. D. Yang
Department of Biochemistry and Molecular Biology, Harbin Medical University
Harbin 150081 (China)
E-mail: dan_yang_hmu@163.com

Dr. L. Gong,[+] Prof. Dr. L. Dong
School of Materials Science and Chemical Engineering, Harbin University of Science and Technology
Harbin 150080 (China)

Prof. Dr. W. Zhao
Heilongjiang University of Chinese Medicine
Harbin 150040 (China)

Prof. Dr. L. Hao, Dr. S. Li
The Plastic and Cosmetic Surgery Center, The first Affiliated Hospital of Harbin Medical University
Harbin 150000 (China)

Prof. Dr. B. Pang
College of Bioinformatics Science and Technology, Harbin Medical University
Harbin 150081 (China)

Prof. Dr. B. Zhou
Key Laboratory for Photonic and Electronic Bandgap Materials, Ministry of Education, Harbin Normal University
Harbin 150025 (China)
E-mail: zhou_bai_bin@163.com

[+] These authors contributed equally to this work.

Supporting information and the ORCID identification number(s) for the author(s) of this article can be found under: https://doi.org/10.1002/anie.202107265.

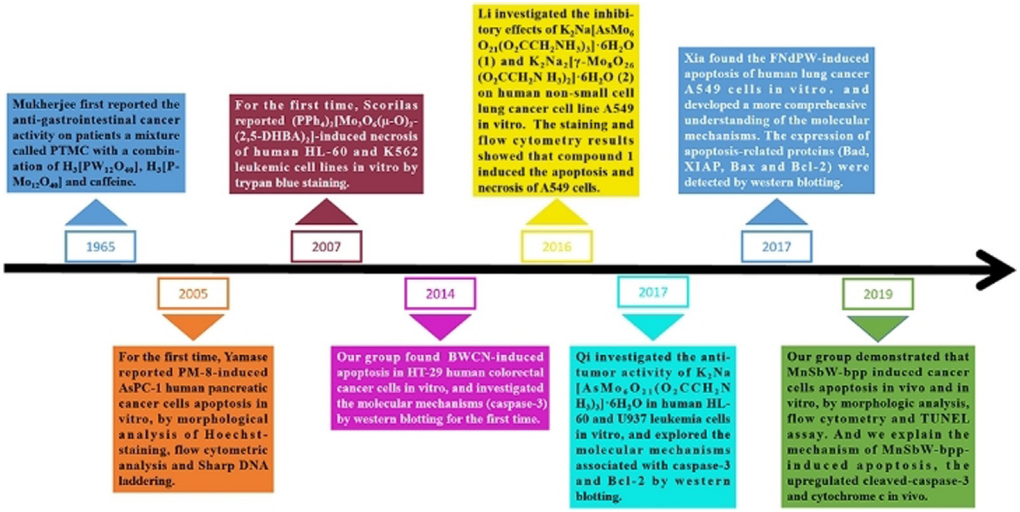

Figure 1. Summary of major events involved in the anticancer activity via cell death of POMs.

Our previous study revealed that trilacunary Keggin-type POMs increased intracellular reactive oxygen species (ROS) levels and consequently inhibited the proliferation of *Tetrahymena thermophiles*.[22] We demonstrated for the first time the involvement of increased ROS in the antiproliferative ability of POMs at the intracellular and molecular level. Generally, ROS levels in cancer cells are much higher than those in normal cells due to abnormal metabolism in cancer cells. To survive, cancer cells dynamically supply reducing equivalents to clear ROS and maintain a normal redox balance. Once the redox balance is disrupted, the increased ROS levels cause macromolecular damage and cancer cell death.[23]

In this study, we report a novel **{BiW$_8$}** compound known as $(Hdmap)_3[\{CoNa_2(H_2O)_8(BiWO_3)\}\{BiW_8O_{30}\}]\cdot 2H_2O$ (dmap = N-(4-pyridyl)dimethylamine) synthesized using a one-step synthesis method. For the first time, we identified pyroptosis to be a new mechanism involved in POM-induced cancer cell death. It was also observed to induce upregulation of ROS levels in MG63 cells. Moreover, we identified multiple antitumor mechanisms involved in the action of **{BiW$_8$}**. Our findings provide a novel and integrative insight into the antitumor mechanism of POMs, with important theoretical and practical significance for drug research on POMs.

Results and Discussion

The chemical formula of the POM examined in this study is $(Hdmap)_3[\{CoNa_2(H_2O)_8(BiWO_3)\}\{BiW_8O_{30}\}]\cdot 2H_2O$ (abbreviated as **{BiW$_8$}**). This compound is a triclinic system with a $P\bar{1}$ space group identified using X-ray single crystal diffraction analysis (Table S3,4). It consists of a $\{B\text{-}\beta\text{-}BiW_8O_{30}\}^{9-}$ anion, a unique 5-nucleated heterometallic unit $\{CoNa_2(H_2O)_8\,(BiWO_3)\}$, and three protonated dmap organic molecules (Figure S1). The $\{B\text{-}\beta\text{-}\,BiW_8O_{30}\}^{9-}$ anion is derived from a three-vacant $[B\text{-}\beta\text{-}BiW_9O_{33}]^{9-}$ group by removal of the WO_6 octahedra. Bi(1) is located at the independent inversion center that forms a three-coordinated structure with five oxygen atoms (four oxygen atoms are semi-occupied) and further connects with eight tungsten ions to form the $\{B\text{-}\beta\text{-}BiW_8O_{30}\}^{9-}$ anion.

The **{BiW$_8$}** sandwich structure is composed of two centrosymmetric $\{B\text{-}\beta\text{-}BiW_8O_{30}\}^{9-}$ polyoxoanions with a special 10-nuclear heterometallic oxygen cluster unit $\{Co_2Na_4(H_2O)_2\,(Bi_2W_2O_5)\}$ derived from two 5-nuclear heterometallic oxygen cluster units $\{CoNa_2(H_2O)_8(BiWO_3)\}$ (Figure 2 a,b). There are four classes of crystallographically independent ions in this unique multinuclear sandwich structure: Bi(2), W(6), Co(1), Na(1), and Na(2). Bi(2) is located at the waist of the sandwich structure and is connected to six oxygen atoms (each oxygen atom is semi-occupied) to form a three-coordinated coordination structure. The octahedral geometry of W(6) is connected with three oxygen atoms in $\{B\text{-}\beta\text{-}BiW_8O_{30}\}^{9-}$ and three oxygen atoms in the nuclear hetero-metal units. Co(1) connects with two oxygen atoms in two different $\{B\text{-}\beta\text{-}BiW_8O_{30}\}^{9-}$ anions, three oxygen atoms in a 5-nuclear hetero-metal unit, and one water molecule to form an octahedral coordination structure. Na(1) forms a bridging coordination structure with oxygen atoms from the 5-nucleated heterometal unit. Six oxygen atoms coordinated with Na(2) come from two oxygen atoms of a 5-nuclear hetero-metal unit and four water molecules. Each 10-core structural unit forms an infinite one-dimensional chain

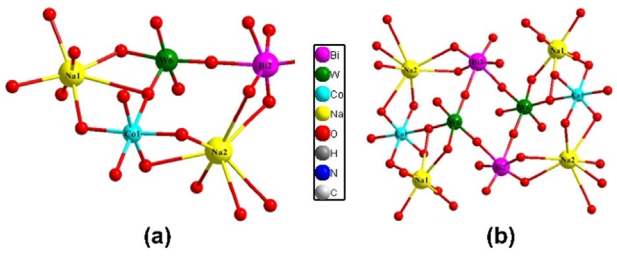

Figure 2. a) 5-nuclear heterometallic oxygen cluster unit; b) a special 10-nuclear hetero-metallic oxygen cluster unit.

through Na(2)-connected μ-O atoms (Figure S2) and a lantern-type two-dimensional sandwich structure through Na(1)-connected μ-O atoms (Figure S3). Some literature[24] have reported that the antitumor activity of POMs is associated with its antioxidant capacity, and the formation of the 10-core hybrid metallic clusters favors the transfer of electrons to enhance the antioxidant reduction capacity of the **{BiW$_8$}** compound. In the stacking arrangement, the adjacent two-dimensional layers are connected by hydrogen bonds (Table S5) and supramolecular interactions between the 4-dimethylaminopyridine groups and oxygen atoms on the surface polyoxoanions to form a 3D structure (Figure S4a). Meanwhile, the compound has a new topological structure with a topological number of $\{0\}_6\{4^{11}.6^8.8^2\}_2\{4^{18}.6^{12}.12^4.14^{18}.16^{13}.18\}\{4^3\}_2\{4^4.12^4.14^2\}_2\{4^6\}_2$-$\{4^7.6^3\}_2\{4\}_{12}$. In the simplified diagram 3D structure, the organic ligands form multiple channels between the lantern-like 2D structures, providing structural support to increase its oxidative reduction (Figure S4b and Figure S5).

Figure S6 shows the infrared absorption spectra of the **{BiW$_8$}** compound, displaying four absorption bands at 727 cm^{-1}, 781 cm^{-1}, 847 cm^{-1}, and 952 cm^{-1} which correspond to the stretching vibration absorptions of $[BiW_8O_{30}]^{9-}$ anions for ν(W-O$_c$-W), ν(W-O$_b$-W), ν(Bi-O$_a$), and ν(W=O$_d$), respectively, in the range of 500–1000 cm^{-1}, which is consistent with previous literature.[25] Moreover, there are three absorption peaks around 1627–2366 cm^{-1}, which can be attributed to the vibrational absorption peaks of the dmap organic ligands in the **{BiW$_8$}** compound.

The thermal stability curve of the **{BiW$_8$}** compound is a two-step weight loss process, as shown in Figure S7. The weight loss rate at the first weight loss step was 6.15 % (theoretical value: 5.56 %) at 95–300 °C, which corresponds to the loss of coordination and lattice water molecules. The weight loss rate at the second weight loss step was 11.61 % (theoretical value: 11.40 %) at 423–675 °C, which corresponds to the loss of dmap organic ligands.

The X-ray spectra of the **{BiW$_8$}** compound showed that the single-crystal simulated diffraction data are consistent with the peak patterns and positions of the actual diffraction patterns, indicating that the **{BiW$_8$}** compound was pure phase (Figure S8). However, the slight difference in peak intensity may be due to the preferred orientation of the crystal plane.

The stability of the **{BiW$_8$}** compound in PBS buffer was obtained via UV spectroscopy after 0, 24, and 48 h of incubation (pH 7.4) at 37 °C. The spectral peaks at 200–300 nm were assigned to the charge transfer transition of O$_d$→W and O$_b$,O$_c$→W[13] in Figure S9. No significant changes were found in the UV spectra after 0, 24, and 48 h, indicating that the compound was stable in aqueous solution and analyzable at room temperature.

The dynamic light scattering spectra (DLS) of 0.5 mM **{BiW$_8$}** compound in PBS buffer (pH 7.4) after 0, 24, and 48 h incubation (pH 7.4) at 37 °C are shown in Figures S10–12. The average particle size of the **{BiW$_8$}** compound was about 6.7–7.4 nm. Furthermore, the particle size did not change significantly after 48 h, indicating that the **{BiW$_8$}** compound is stable in PBS buffer.

To determine the effect of **{BiW$_8$}** on cell proliferation, the cell viabilities of one normal cell line (human umbilical vein endothelial cell line [HUVEC]) and five carcinoma cell lines (human osteosarcoma cell line, MG63; human rhabdomyosarcoma cell line, RD; human liver cancer cell lines, HepG2 and Hep3B; and human breast carcinoma cell line, MCF7) were measured via MTT assays (Figure S13,14). At 24 h post-incubation, the half maximal inhibitory concentrations (IC$_{50}$) values of **{BiW$_8$}** against HUVEC, MG63, RD, Hep3B, HepG2, and MCF7 cells were 895.8, 127.3, 344.3, 455.0, 781.3, and 206.3 μM, respectively (Table S6). At 48 h post-incubation, their IC$_{50}$ values were 381.6, 63.2, 164.3, 217.1, 288.1, and 84.3 μM, respectively. Drug screening showed that cell proliferation in the MG63 cells was the most pronounced. Therefore, we selected MG63 cells for further studies.

The growth inhibition in MG63 cells treated with **{BiW$_8$}** and three raw materials ($Na_2WO_4{\cdot}2H_2O$, $CoCl_2{\cdot}6H_2O$, and dmap) for 24 and 48 h was measured (Figure 3, S15, and S16). At 24 h post-incubation, the IC$_{50}$ values of **{BiW$_8$}**, $Na_2WO_4{\cdot}2H_2O$, $CoCl_2{\cdot}6H_2O$, and dmap were 127.3, 1003.0, 11 596.2, and 365.5 μM, respectively (Table S7). At 48 h post-incubation, their IC$_{50}$ values were 63.2, 298.9, 648.3, and 115.9 μM, respectively. The inhibitory effects **{BiW$_8$}** on the MG63 cells were higher than those of the other three raw

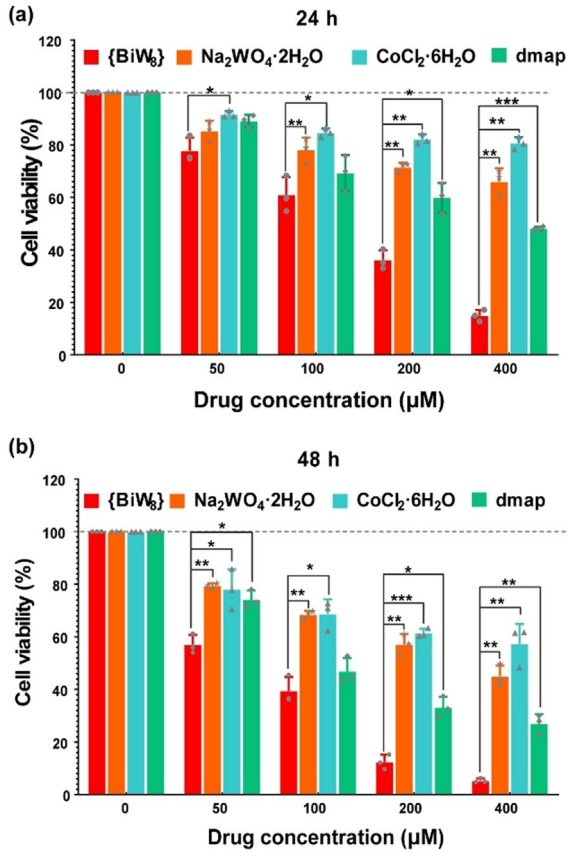

Figure 3. MTT assay analysis on the MG63 cells treated with **{BiW$_8$}** and three raw materials with the indicated concentrations for a) 24 h ($n=3$) and b) 48 h ($n=3$). Data are presented as the mean ± SD. Statistical significances were calculated using Student's t-test or two-way ANOVA, $*p<0.05$, $**p<0.01$, or $***p<0.001$.

materials at the same time points. In addition, our data (Figure S17,18, Table S8) showed that **{BiW_8}** exhibited higher anticancer activity than three other POM drugs ($Na_9[SbW_9O_{33}]\cdot 19.5H_2O$, $Na_6H_4[Bi_2W_{20}Co_2O_{70}(H_2O)_6]\cdot 34H_2O$, and $Na_9[BiW_9O_{33}]\cdot 16H_2O$). This may be due to the organically functionalized dmap and 10-core hybrid metallic clusters that favor the transfer of electrons, enhancing its antioxidant reduction capacity.

In addition to excessive cell proliferative ability of cancer malignancies, invasion and migration abilities have also been identified as classic hallmarks.[26] To evaluate the impact of **{BiW_8}** on the migration and invasion of MG63 cells, a wound healing assay (Figure S19) and Transwell Matrigel assay (Figure S20) were performed. Results indicate that **{BiW_8}** repressed the migration and invasion abilities of the MG63 cells. Due to these findings on the anti-proliferation, anti-migration, and anti-invasion abilities of **{BiW_8}**, more detailed evidence on the effects of **{BiW_8}** against cancer were explored.

To characterize the morphologic changes induced by **{BiW_8}**, we acquired transmission electron microscopy (TEM) images of MG63 cells before and after incubation with **{BiW_8}** (Figure 4). When treated with 127.3 μM **{BiW_8}** for 24 h, the MG63 cells exhibited cell swelling, pyknosis of the nucleoli, and central localization of the nuclei (Figure 4b). As the duration of **{BiW_8}** administration increased (Figure 4c), the MG63 cells exhibited more striking changes in cell morphology, such as disintegrated cell membranes, nuclear condensation, loss of nucleoli, and lysis of organelles. According to previous studies, POMs usually induce cancer cell apoptosis,[27] which is characterized by a decrease in cell volume, shrinkage of the cytoplasm, formation of membrane-bound apoptotic bodies, and well-preserved but compacted cytoplasmic organelles.[18] Our ultrastructural observations revealed a clear difference in morphology between apoptosis and the observed **{BiW_8}**-induced cell death. Based on the morphology results, we speculate that **{BiW_8}** may induce pyroptosis.

To identify the type of cell death induced by **{BiW_8}**, a lactate dehydrogenase (LDH) release assay and adenosine triphosphate (ATP) assay were performed since they measure hallmarks of pyroptosis (Figure 5). MG63 cells were treated with 127.3 μM **{BiW_8}** for 24 and 48 h, and levels of released LDH in the culture supernatants were measured (Figure 5a). As treatment duration was extended, compared with control group ($150.6 \pm 5.831\ U\,L^{-1}$), increased extracellular release of LDH was observed in the experimental group ($513.5 \pm 25.34\ U\,L^{-1}$ and $593.5 \pm 13.60\ U\,L^{-1}$ after 24 and 48 h, respectively), reflecting the induction of cell death. In contrast, compared with the control group ($100.0 \pm 0.0\%$), reduced ATP levels were observed in the experimental group ($46.85 \pm 1.939\%$ and $25.44 \pm 0.2321\%$ at 24 and 48 h, respectively), reflecting the reduction of cell vitality (Figure 5b).

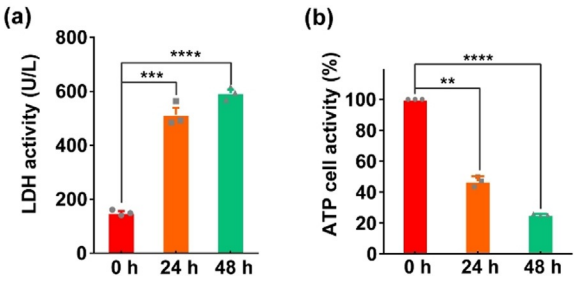

Figure 5. LDH release and ATP assays. a) Before incubation as well as after incubation with 127.3 μM **{BiW_8}** for 24 and 48 h, cell death was determined by measuring LDH release in the culture supernatants; b) Before incubation as well as after incubation with 127.3 μM **{BiW_8}** for 24 and 48 h, cell viability was determined by measuring ATP levels in MG63 cells. Data are shown as mean ± SD of three independent experiments. Statistical significances were calculated using Student's t-test or one-way ANOVA, $^{**}p < 0.01$, $^{***}p < 0.001$, $^{****}p < 0.0001$.

Considering the experimental results of the TEM morphology, LDH release assay, and ATP assay, we confirmed that **{BiW_8}** induced pyroptosis. To our knowledge, this is the first time that POMs have been identified to induce cancer cell pyroptosis, providing a new insight into the antitumor mechanism of POMs.

An earlier study demonstrated that POM toxicity was strictly dependent on increased ROS levels in *Tetrahymena thermophile*.[22] Hence, the changes in ROS levels in MG63 cells induced by **{BiW_8}** are of interest. Quantification of the DCF staining results (Figure 6) showed that the ROS levels in the experimental group were twice those in the control group. It is known that intercellular ROS levels are dynamic,

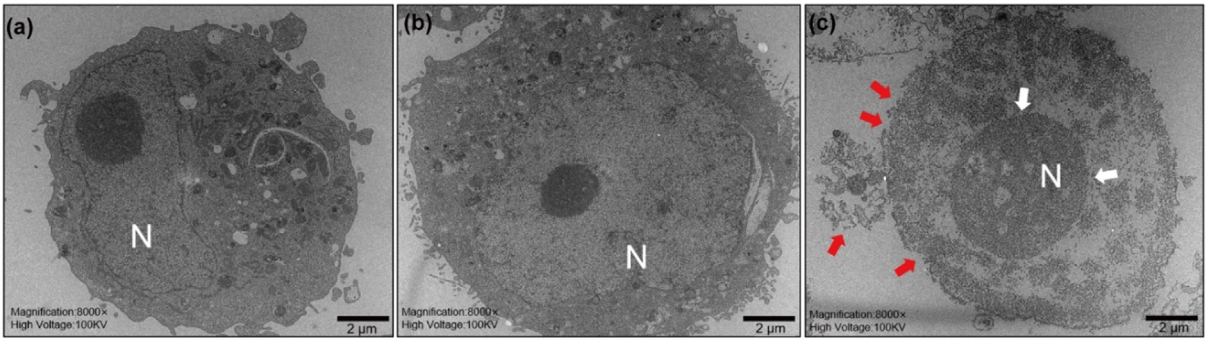

Figure 4. Cell morphology visualization by transmission electron microscopy (TEM). a) Representative morphology of the normal MG63 cells; b) Representative morphology of the MG63 cells treated with 127.3 μM **{BiW_8}** for 24 h; c) Representative morphology of the MG63 cells treated with 127.3 μM **{BiW_8}** for 48 h. The red arrows indicate the ruptured cell membrane and content leakage, while the white arrows indicate nuclear condensation and loss of nucleoli. Magnification 8000×, high voltage 1000 kV, Scale bars = 2 μm.

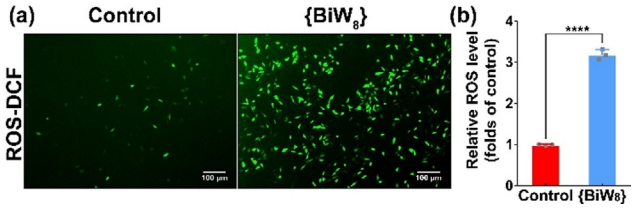

Figure 6. Effects of **{BiW$_8$}** on intracellular ROS levels. a) A ROS assay was applied to detect the oxidative state of the MG63 cells. The experimental group was treated with 127.3 μM **{BiW$_8$}** for 24 h, while control group was cultured under normal conditions, scale bars = 100 μm; b) Quantification of ROS wherein relative ROS levels in the experimental group were normalized to the control group. Data are shown as the mean ± SD of three independent experiments. Statistical significances were calculated using Student's t-test, ****$p < 0.0001$.

determined by the balance between ROS production and clearance. Given that ROS inhibition is a major action of glutathione (GSH), we tested the effect of **{BiW$_8$}** on GSH levels in both cellular and chemical milieu.

GSH and NADPH catalyzed by glutathione reductase (GR) produce GSSG and NADP, respectively (Figure 7a).[28] Real-time monitoring of this reaction was performed by measuring the UV absorption peak of NADPH at 340 nm.[29] The addition of **{BiW$_8$}** showed no activity in the absence of any of the components (Figure 7b), indicating that **{BiW$_8$}** did not possess nor inhibit glutathione peroxidase (GPX) or GR enzyme activities. However, the NADPH absorbance decreased significantly after the addition of **{BiW$_8$}** when all the components in the system were present.

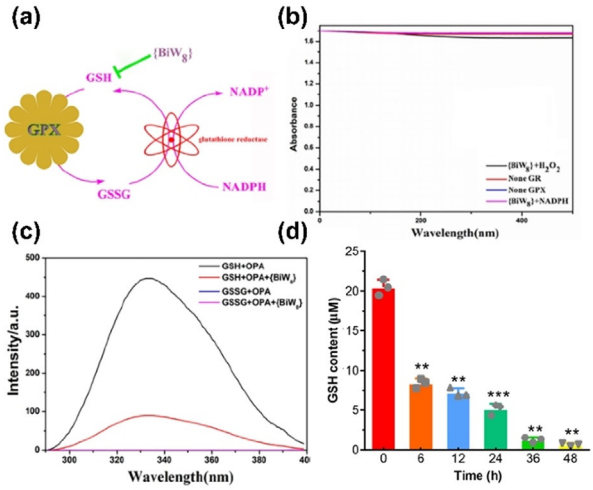

Figure 7. a) The schematic illustration for the relationship between **{BiW$_8$}** and GSH; b) The study of GSH activity for **{BiW$_8$}**: **{BiW$_8$}** (3 mM), GSH (2 mM), NADPH (0.4 mM), GPX (2.0units), GR (1.7 units), H_2O_2 (240 μM) in 25 mM pH 7.4 phosphate buffer at 25 °C. c) The fluorescence spectra of **{BiW$_8$}**, GSH and OPA:**{BiW$_8$}** (3 mM), GSH(2 mM), GSSG(2 mM) and OPA(10 mM) were studied using fluorescence analysis ($\lambda_{ex} = 334$. 4 nm, $\lambda_{em} = 424$ nm); d) GSH assay, GSH content of MG63 cells before incubation and after 6, 12, 24, 36 and 48 h incubation with 127.3 μM **{BiW$_8$}**. Data are shown as mean ± SD of three independent experiments. Statistical significances were calculated using Student's t-test, ** $p < 0.01$, *** $p < 0.001$.

As shown in Figure S21a, the absorbance of the NADPH decreases significantly with the increase of **{BiW$_8$}** concentration and The concentration of **{BiW$_8$}** showed a nonlinear relationship with the inhibition rate according to the equation $Y = 0.573x^{1.309}/(0.569 + x^{1.309})$, where Y is inhibition rate of NADPH, and X is the concentration of **{BiW$_8$}** (Figure S21b). The inhibition rate was 6.06 % for $IC_{50} = 127.30$ μM. Meanwhile, 3 mM **{BiW$_8$}** demonstrated excellent inhibition (51.22 %) compared with the three raw materials (Figure S22). These results suggest that **{BiW$_8$}** may react with GSH or GSSG to alter the production of NADPH.

To explore whether **{BiW$_8$}** reacted with GSH and GSSG, we conducted the following experiments. GSH was condensed at pH 8.0 with the two aldehyde groups of *o*-phthalaldehyde (OPA) to form isoindole (GSH-OPA), a strong fluorescent substance ($\lambda_{ex} = 334$. 4 nm, $\lambda_{em} = 424$ nm). The fluorescence (Figure 7c) decreased after adding **{BiW$_8$}**, indicating that it reacted with GSH and inhibited the reaction with OPA. On the other hand, GSSG rarely binds to OPA to produce fluorescent substances at pH 8.0. The fluorescence value for the substances produced by this reaction did not change after adding **{BiW$_8$}**, indicating that it did not react with GSSG. To explore whether **{BiW$_8$}** affects the levels of GSH, GSSG, and total glutathione (T-GSH) in MG63 cells, a GSH assay was performed. Compared with the intracellular GSH content at 0 h, the GSH content decreased by 59 %, 65 %, 75 %, 94 %, and 97 % at 6, 12, 24, 36 and 48 h, respectively (Figure 7d). Additionally, the T-GSH and GSSG after 48 h of incubation with **{BiW$_8$}** were reduced by 97 % and 95 % compared to 0 h, respectively (Figure S23). The downregulation of intracellular GSH, T-GSH, and GSSG content was consistent with the chemical reaction results.

However, it is still unclear how **{BiW$_8$}** induces pyroptosis, increases intracellular ROS, and decreases intracellular GSH in MG63 cells. Thus, we performed RNA sequencing. Compared with the control group, 3737 upregulated and 3396 downregulated differentially expressed genes (DEGs), were identified in the experimental group (MG63 cells were treated with 127.30 μM **{BiW$_8$}** for 24 h). The DEGs are represented in a standard volcano plot (Figure S24a) and heatmap (Figure S24b).

To outline the potential functions of the DEGs, we performed functional enrichment analysis of the top 3000 upregulated and downregulated DEGs. A total of 20 Gene Ontology (GO) terms of biological process (BP), 14 GO terms of cellular component (CC), 9 GO terms of molecular function (MF), and 24 Kyoto Encyclopedia of Genes and Genomes (KEGG) pathways were identified (Figure 8, S25). When the cutoff was to the top 3000 downregulated DEGs, 14 KEGG pathways were identified (Figure S26). In addition, nearly all genes enriched in the KEGG pathway annotations of mismatch repair, base excision repair, DNA replication, cell cycle, and glutathione metabolism were from the top 3000 downregulated DEGs. This suggests that **{BiW$_8$}** impaired DNA repair, replication, and glutathione metabolism in the MG63 cells.

We then searched literature for the DEGs. As shown in Table 1 and S9, 21 downregulated DEGs were involved in DNA repair and replication, 13 downregulated DEGs were

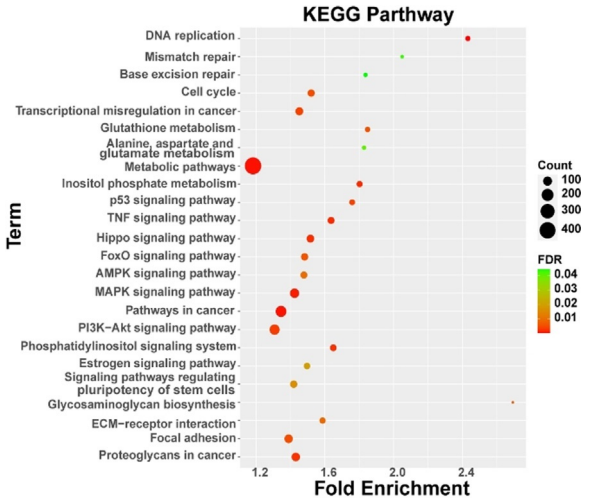

Figure 8. Bubble diagram of the KEGG pathway analysis enriched by 3000 upregulated and downregulated DEGs (experimental group vs. control group, FDR < 0.05). The colors of the nodes reflect the FDR values of the designated pathways, and the sizes of the nodes indicate the number of DEGs enriched in the pathways.

Table 1: DEGs in RNA-sequencing (experimental vs. control group, | Log2FoldChange | > 0.58, adj. $p < 0.05$.).

Category	Gene symbol
DNA repair/ replication (down-regulated)	APEX1, APEX2, EXO1, FEN1, LIG1, MSH2, MSH3, MUTYH, NEIL2, NTHL1, OGG1, PARP1, PCNA, POLD1, POLD3, POLE, POLE2, RPA1, RPA3, UNG, XRCC1
Glutathione metabolism (down-regulated)	GSTA1, GSTA2, GSTA4, GSTK1, GSTM1, GSTM2, GSTM4, GSTT2B, GPX1, GPX2, GPX4, GPX7, GPX8
Pyroptosis (up-regulated)	CASP3, CASP4, CASP5, GSDMB, GSDME, IL18, NLRP3, NLRC4, NLRP10, TXNIP

involved in glutathione metabolism, and 10 upregulated DEGs were involved in pyroptosis. Quantitative real-time polymerase chain reaction (qRT-PCR) was performed to validate this, showing the DEGs with greater absolute values of fold-change (Figure 9).

We summarized all the antitumor mechanisms of **{BiW$_8$}** in Figure 10. For the first time, we found that POMs induced pyroptosis. Additionally, we explored further possible mechanisms and targets involved in the effects of POMs (Figure 10a). RNA-seq and qRT-PCR results showed that **{BiW$_8$}** increased DEGs encoding proteins associated with pyroptosis, such as the cysteine aspartic acid-specific protease (CASP3, CASP4, and CASP5), gasdermins (GSDMB, GSDME), inflammasome (NLRP3, NLRC4, and NLRP10), and interleukin-18 (IL-18). Given that several chemotherapeutic agents increase intracellular ROS to activate the pyroptosis pathway in cancer cells,[20–21] a possible mechanism for MG63 cell pyroptosis could be mediated through the accumulation of ROS induced by **{BiW$_8$}**. However, further biological and chemical validation of this hypothesis are required.

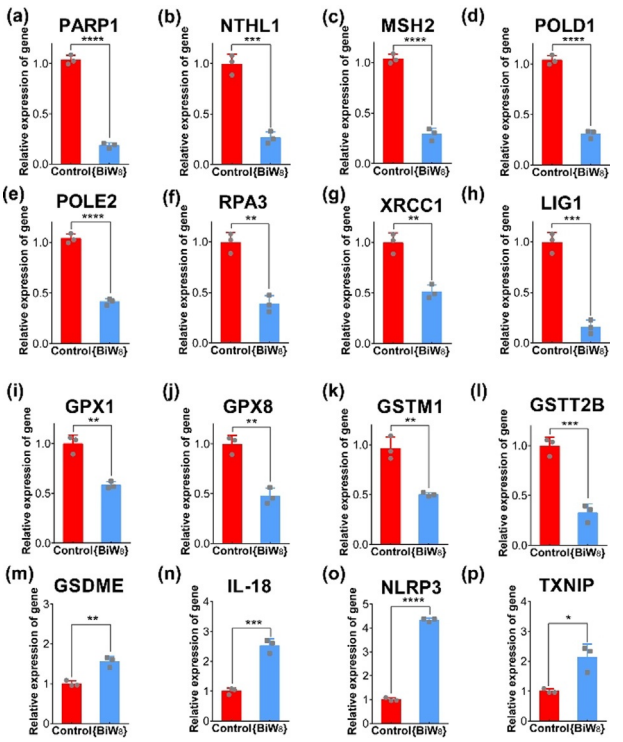

Figure 9. qRT-PCR analysis of the DEGs in the experimental and control groups. a) PARP1; b) NTHL1; c) MSH2; d) POLD1; e) POLE2; f) RPA3; g) XRCC1; h) LIG1; i) GPX1; j) GPX8; k) GSTM1; l) GSTT2B; m) GSDME; n) IL-18; o) NLRP3; and p) TXNIP. Data are shown as mean ± SD of three independent experiments. Statistical significances were calculated using Student's t-test, $*p < 0.05$, $**p < 0.01$, $***p < 0.001$, $****p < 0.0001$.

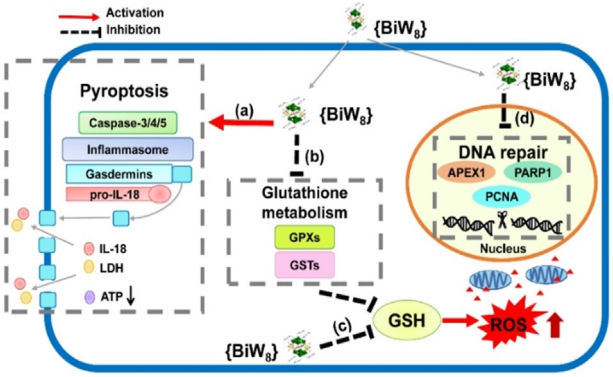

Figure 10. Schematic illustration of the antitumor mechanisms of **{BiW$_8$}**. a) **{BiW$_8$}** induced pyroptosis by upregulating genes associated with pyroptosis, such as cysteine aspartic acid specific protease (CASP3, CASP4, and CASP5), gasdermins (GSDMB, GSDME), inflammasome (NLRP3, NLRC4, and NLRP10), and interleukin-18 (IL-18). **{BiW$_8$}** decreased the intracellular ATP level, and increased the release of LDH; b) **{BiW$_8$}** increased ROS levels and decreased intracellular GSH levels by downregulating genes involved in glutathione metabolism, such as glutathione peroxidases (GPX1 and GPX8) and glutathione S-transferases (GSTM1 and GSTT2B); c) **{BiW$_8$}** increased ROS levels and depleted GSH; d) **{BiW$_8$}** decreased DNA repair/replication enzymes, such as poly (ADP-ribose) polymerase (PARP1), DNA mismatch repair protein (MSH2), and DNA ligase (LIG1).

Additionally, **{BiW_8}** reduced GSH levels in both cellular and chemical milieu and increased ROS levels in MG63 cells. Furthermore, the analysis of the KEGG pathway and qRT-PCR indicated that **{BiW_8}** inhibited the expression of DEGs associated with glutathione metabolism. These genes encode antioxidant proteins involved in GSH regeneration, including glutathione peroxidases (GPX1 and GPX8) and glutathione S-transferases (GSTM1 and GSTT2B). Taken together, the combined effect of **{BiW_8}** through transcriptional repression and chemical reaction decreased GSH levels and consequently increased ROS levels in the MG63 cells (Figure 10b,c).

{BiW_8} also decreased DEGs that encode DNA repair/replication enzymes, such as poly (ADP-ribose) polymerase (PARP1), DNA mismatch repair protein (MSH2), and DNA ligase (LIG1) (Figure 10d). Previous studies have shown that decreased GSH results in ROS accumulation, leading to oxidative damage of DNA and activation of the DNA damage response (DDR) pathway.[30] Depending on the degree of DNA damage, cells are committed to different fates, which range from DNA damage repair to cell death.[31] The excessive ROS-induced DNA damage caused by **{BiW_8}**-induced reduction of GSH levels may have caused the cell death in the MG63 cells. **{BiW_8}** may have the capacity to cause DNA damage and inhibit the DNA repair system in MG63 cells.

Conclusion

In the current study, we successfully synthesized a 10-nuclear heteroatom-modified cluster {BiW_8O_{30}}. **{BiW_8}** exerted cytotoxic effects by suppressing the proliferation, migration, and invasion of MG63 cells. Through various assays, we also demonstrated pyroptosis as a newly identified mechanism of cell death induced by **{BiW_8}**. Decreased GSH content and increased ROS levels were observed in the **{BiW_8}**-treated MG63 cells. Furthermore, multiple antitumor mechanisms of **{BiW_8}** were identified via transcriptome analysis and chemical simulation, including activation of pyroptosis, suppression of GSH generation, depletion of GSH, and inhibition of DNA repair. In summary, our findings provide insight into the development of POMs as antitumor drugs with important theoretical and practical significance for drug research.[32]

Acknowledgements

This work was supported by the National Natural Science Foundation of China (Grants 81272530, 21571044 and 21771046), Training Project for the Young Innovative Talents of Higher Education Institutions in Heilongjiang Province (Grant UNPYSCT-2020084), Research Projects of Basic Scientific Research of Provincial Universities in Heilongjiang Province (Grant 2019-KYYWF-1255), the Science and Technology Plan Project of Qiqihar (Grant LHYD-202001), Doctor Program of the Academy of Medical Sciences of Qiqihar (Grant QMSI2019B-06 and QY2016B-20), the 2020 Central Government's Plan to Support the Talent Training Project of the Reform and Development Fund of Local Universities(1401120002) and the Excellent Scientific Research Team Project of Harbin Normal University (XKYT2020001).

Conflict of Interest

The authors declare no conflict of interest.

Keywords: {BiW_8O_{30}} · antitumor mechanism · pyroptosis · ROS · transcriptome analysis

[1] A. V. Anyushin, A. Kondinski, T. N. Parac-Vogt, *Chem. Soc. Rev.* **2020**, *49*, 382 – 432.
[2] B. Huang, D. H. Yang, B. H. Han, *J. Mater. Chem. A* **2020**, *8*, 4593 – 4628.
[3] S. C. Huang, C. C. Lin, C. T. Hsu, C. H. Guo, T. Y. Chen, Y. F. Liao, H. Y. Chen, *J. Mater. Chem. A* **2020**, *8*, 21623 – 21633.
[4] Y. Zheng, H. Gan, W. Li, Y. Wu, X. Yan, Y. Wang, J. Li, J. Li, X. Wang, *Chem. Eur. J.* **2019**, *25*, 15326 – 15332.
[5] Z. S. Guang, H. Z. Gui, Y. L. Hai, L. Z. Yu, *J. Mol. Struct.* **2019**, *1198*, 126831.
[6] H. Qi, G. Zhu, L. Li, N. Xu, *Chin. J. Chem. Eng.* **2015**, *23*, 31 – 41.
[7] H. X. Zhao, L. Tao, F. M. Zhang, Y. Zhang, Y. Q. Liu, H. J. Xu, G. W. Diao, L. B. Ni, *Chem. Commun.* **2019**, *55*, 1096 – 1099.
[8] M. R. Horn, A. Singh, S. Alomari, S. G. Ferrón, R. B. Vilau, N. Chodankar, N. Motta, K. Ostrikov, J. J. MacLeod, P. Sonar, P. G. Romero, D. Dubal, *Energy Environ. Sci.* **2021**, Advance Article.
[9] H. Soria-Carrera, I. F. Castillo, P. Romero, S. Martín, J. M. de la Fuente, S. G. Mitchell, R. M. Rapún, *Angew. Chem. Int. Ed.* **2021**, *60*, 3449 – 3453; *Angew. Chem.* **2021**, *133*, 3491 – 3495.
[10] E. Benazzi, J. Karlsson, Y. B. M'Barek, P. Chabera, S. Blanchard, S. Alves, A. Proust, T. Pullerits, G. G. Izzet, E. A. Gibson, *Inorg. Chem. Front.* **2021**, Advance Article.
[11] Z. L. Lang, Y. G. Li, A. Clotet, J. M. Poblet, *Catal. Sci. Technol.* **2020**, *10*, 8219 – 8229.
[12] L. Wang, B. B. Zhou, K. Yu, Z. H. Su, S. Gao, L. L. Chu, J. R. Liu, G. Y. Yang, *Inorg. Chem.* **2013**, *52*, 5119 – 5127.
[13] L. Wang, K. Yu, B. B. Zhou, Z. H. Su, S. Gao, L. L. Chu, J. R. Liu, *Dalton Trans.* **2014**, *43*, 6070 – 6078.
[14] L. Wang, K. Yu, J. Zhu, B. B. Zhou, J. R. Liu, G. Y. Yang, *Dalton Trans.* **2017**, *46*, 2874 – 2883.
[15] a) W. X. Zhao, C. H. Wang, S. F. Dong, Y. Li, D. Zhang, L. Q. Han, *Int. Conf. Hum. Health Biomed. Eng.* **2011**, 594 – 597; b) H. Y. Liu, X. L. Pan, J. N. Tian, H. Sun, Q. Huan, Y. L. Huang, J. Q. Liu, *Oncol. Lett.* **2017**, *13*, 2418 – 2424.
[16] E. Koren, Y. Fuchs, *Cancer Discovery* **2021**, *11*, 245 – 265.
[17] a) H. Zafar, F. Raza, S. Y. Ma, Y. Wei, J. Zhang, Q. Shen, *Biomater. Sci.* **2021**, *9*, 5092 – 5115; b) H. Wang, D. F. Lin, Q. Q. Yu, Z. Q. Li, C. Lenahan, Y. Dong, Q. C. Wei, A. W. Shao, *Front. Cell. Dev. Biol.* **2021**, https://doi.org/10.3389/fcell.2021.629150; c) Y. X. Tan, Q. Z. Chen, X. L. Li, Z. Y. Zeng, W. Xiong, G. Y. Li, X. Y. Li, J. B. Yang, B. Xiang, M. Yi, *J. Exp. Clin. Cancer Res.* **2021**, *40*, 153.
[18] a) R. S. Hotchkiss, A. Strasser, J. E. McDunn, P. E. Swanson, *N. Engl. J. Med.* **2009**, *361*, 1570 – 1583; b) L. Galluzzi, I. Vitale, et al., *Cell. Death. Differ.* **2018**, *25*, 486 – 541.
[19] Y. P. Wang, W. Q. Gao, X. Y. Shi, J. Q. Ding, W. Liu, H. B. He, K. Wang, F. Shao, *Nature* **2017**, *547*, 99 – 103.
[20] X. W. Zhang, P. Zhang, L. An, N. Y. Sun, L. Y. Peng, W. W. Tang, D. Y. Mac, J. Chena, *Acta Pharm. Sin. B* **2020**, *10*, 1397 – 1413.
[21] a) J. F. Teng, Q. B. Mei, X. G. Zhou, Y. Tang, R. Xiong, W. Q. Qiu, R. Pan, B. Y. Law, V. K. Wong, C. L. Yu, H. A. Long, X. L. Xiao, F. Zhang, J. M. Wu, D. L. Qin, A. G. Wu, *Cancers* **2020**, *12*,

193; b) Y. Yang, P. Y. Liu, W. Bao, S. J. Chen, F. S. Wu, P. Y. Zhu, *BMC Cancer* **2020**, *20*, 28.
[22] L. G. Gong, W. Q. Ding, Y. Chen, K. Yu, C. H. Guo, B. B. Zhou, *Angew. Chem. Int. Ed.* **2021**, *60*, 8344 – 8351; *Angew. Chem.* **2021**, *133*, 8425 – 8432.
[23] N. M. Grüning, M. Ralser, *Nature* **2011**, *480*, 190 – 191.
[24] a) T. Yamase, *Mol. Eng.* **1993**, *3*, 241 – 262; b) Y. Liu, S. Tian, S. Liu, E. Wang, Y. Y. Liu, S. Y. Tian, S. X. Liu, E. B. Wang, *Transit. Met. Chem.* **2005**, *30*, 113 – 117.
[25] L. L. Li, H. Y. Han, Y. H. Wang, H. Q. Tan, H. Y. Zang, Y. G. Li, *Dalton Trans.* **2015**, *44*, 11429 – 11436.
[26] D. Hanahan, R. A. Weinberg, *Cell* **2011**, *144*, 646 – 674.
[27] Z. M. Zhang, X. Duan, S. Yao, Z. Wang, Z. Lin, Y. G. Li, L. S. Long, E. B. Wang, W. Lin, *Chem. Sci.* **2016**, *7*, 4220 – 4229.
[28] Y. Huang, Z. Liu, C. Liu, E. Ju, Y. Zhang, J. Ren, X. Qu, *Angew. Chem. Int. Ed.* **2016**, *55*, 6646 – 6650; *Angew. Chem.* **2016**, *128*, 6758 – 6762.
[29] A. A. Vernekar, D. Sinha, S. Srivastava, P. U. Paramasivam, P. D'Silva, G. Mugesh, *Nat. Commun.* **2014**, *5*, 5301 – 5313.
[30] J. N. Moloney, T. G. Cotter, *Semin. Cell Dev. Biol.* **2018**, *80*, 50 – 64.
[31] a) S. Matt, T. G. Hofmann, *Cell. Mol. Life Sci.* **2016**, *73*, 2829 – 2850; b) W. P. Roos, A. D. Thomas, B. Kaina, *Nat. Rev. Cancer* **2016**, *16*, 20 – 33.
[32] Deposition Number(s) 1830842 contain(s) the supplementary crystallographic data for this paper. These data are provided free of charge by the joint Cambridge Crystallographic Data Centre and Fachinformationszentrum Karlsruhe Access Structures service www.ccdc.cam.ac.uk/structures.

Manuscript received: May 31, 2021
Revised manuscript received: July 2, 2021
Accepted manuscript online: July 27, 2021
Version of record online: August 20, 2021

